

pubs.acs.org/JPCL Letter

# Influence of Halogen-Solvent Hydrogen Bonding on Gold Nanocluster Photoluminescence

Daniel J. Heintzelman, Seth A. Nelson, and Kenneth L. Knappenberger, Jr.\*



Cite This: J. Phys. Chem. Lett. 2024, 15, 2951-2956



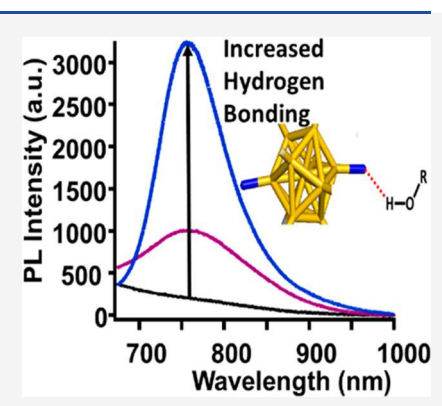
ACCESS I

III Metrics & More

Article Recommendations

sı Supporting Information

**ABSTRACT:** The influence of gold nanocluster—solvent interactions on nanostructure optical properties was determined. Using  $[Au_{11}(BINAP)_4X_2]^+$ , where X = Cl or Br, as a model system, the dramatic influence of halogen—solvent hydrogen bonding on nanocluster optical properties was resolved. The creation of a nanocluster—solvent hydrogen-bond network yielded intense photoluminescence (PL) and an accompanying 2-fold reduction in vibration-mediated nonradiative decay rates. PL was quenched for systems that did not support hydrogen bonding. As reflected by absorption line widths, Raman scattering, and transient absorption spectroscopy measurements, the hydrogen-bond network increased nanocluster structural rigidity and reduced nonradiative carrier decay rates. The results highlight the significant role of the nanocluster—solvent interface in determining the properties of structurally precise materials.



S ubnanometer to few-nanometer metal nanoclusters exhibit optical, electronic, and mechanical properties that are distinct from those of even slightly larger plasmonic nanoparticles. These systems' unique characteristics and high degree of structural precision provide opportunities to tailor energy-transfer pathways and efficiencies. As a result, structurally precise nanoclusters can impact applications such as photodynamic therapy, manufacturing of materials, mass sensing, optical tagging, photonic integrated circuits, quantum emitters, etc.

Monolayer-protected clusters (MPCs) are colloidal metals that are synthesized and isolated with a high degree of structural precision (in some cases, atomic precision). To MPC properties are intimately linked to the structure. MPCs are generally composed of three distinct structural motifs: (1) an all-metal core, (2) a metal-organic interface, and (3) organic ligands that passivate the cluster. 18 Phosphine-protected clusters are a particularly interesting subset of MPCs. These clusters are especially malleable, with ligand substitutions causing significant deformations to the MPC core structure. 19,20 Replacement of monodentate phosphine ligands with bidentate ones transforms the normally achiral cluster to a chiral geometry.<sup>19</sup> The chiral cluster shows rich circular dichroism (CD) spectra, spanning ultraviolet-visible (UVvis) frequencies. 19,21,22 Because in the bidentate case the same ligand is bound to the gold core at two sites, strain is imparted onto the gold kernel and in turn alters the bond lengths and rigidity of the metal. Density functional theory (DFT) calculations also indicate that ligands that passivate these clusters have a significant impact on the electronic structure and chiroptical properties of the gold core.<sup>20,23</sup>

The  $[Au_{11}(BINAP)_4X_2]^+$  MPC, where X represents axial chlorine or bromine atoms, provides access to gold-halogen bonds for influencing nanocluster optical properties, a structural parameter that has not yet been exploited. Halogen atoms are essential to Au<sub>11</sub> stability. Because the gold core carries an overall charge of +3 and the phosphine ligands do not donate charge, the halogens provide a route to charge neutralization, aiding both crystalline and solution phase stability.<sup>19</sup> Furthermore, a third halogen (either chloride or bromide depending on the MPC) acts as a counterion to stabilize the MPC. Monophosphine-protected Au<sub>11</sub> clusters emit near-infrared (NIR) photoluminescence (PL) consisting of multiple peaks.<sup>24</sup> However, PL studies of bidentate phosphine-protected Au<sub>11</sub> clusters have not been reported. Thus, the influence of the ligand shell, including axial halogens, on the gold MPC optical properties is not fully understood.

Here, we describe the influence of cluster–solvent interactions on the electronic absorption, photoluminescence, and ultrafast relaxation dynamics of  $[Au_{11}(R/S-BINAP)_4X_2]^+$  MPCs. Using a combination of femtosecond time-resolved transient absorption (fs-TA), UV–vis absorption, Raman, and emission spectroscopy measurements, the ability of  $[Au_{11}(R/S-BINAP)_4Cl_2]^+$  to hydrogen bond with protic solvents is uncovered. The formation of a gold–chlorine–hydrogen bond

Received: January 19, 2024
Revised: February 29, 2024
Accepted: March 5, 2024
Published: March 7, 2024





leads to increased cluster rigidity. As a result, cluster—solvent hydrogen bonding decreases vibrationally mediated relaxation lifetimes and increases PL emission rates. The results are halogen specific and highlight the importance of axial halogens not only for aiding MPC stability but also for determining nanocluster physical properties.

The UV-vis absorption spectra for both  $[Au_{11}(R/S-BINAP)_4X_2]^+$  MPCs dispersed in toluene are shown in Figure 1a. For both MPCs, major features were present at 560, 470,

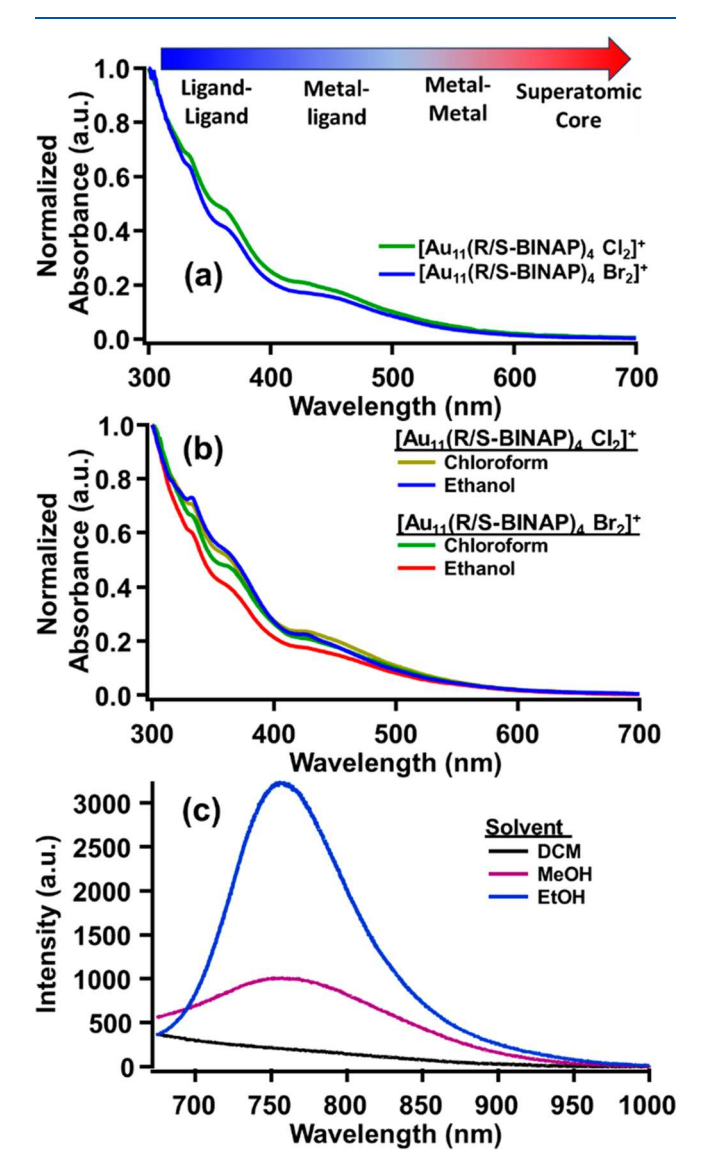


**Figure 1.** (a) UV–vis absorption spectra of  $[Au_{11}(R/S-BINAP)_4X_2]^+$  in toluene. The arrow at the top generalizes the wavelength-dependent structural origin of the electronic transitions. (b) UV–vis absorption spectra of  $[Au_{11}(R/S-BINAP)_4X_2]^+$  dispersed in protic (ethanol) and aprotic (chloroform) solvents. (c) Emission spectrum of  $[Au_{11}(R/S-BINAP)_4Cl_2]^+$  in different solvents (532 nm excitation).

430, 360, and 330 nm. These spectra, along with electrospray ionization mass spectrometry (ESI-MS) data (Figure S1), agreed with previous results. The absorption transitions are assigned using DFT calculations. Peaks at wavelengths of >440 nm originate from core-based excitations. The lowest-energy transitions result from superatomic gold states. Peaks at wavelengths of <440 nm are from a mix of the core and

ligand states. The general structure- and wavelength-dependent trends of  $[\mathrm{Au}_{11}(\mathrm{R/S\text{-}BINAP})_4\mathrm{X}_2]^+$  absorption are summarized in Figure 1a (top). The primary difference was a change in absorbance for 305 nm  $\leq \lambda \leq$  450 nm, where metal—ligand interactions dominate; the chlorinated cluster is a slightly stronger absorber. Tsukuda et al. previously described the differences in absorption between these nanoclusters, reporting molar extinction coefficients of 3.4  $\times$  10<sup>5</sup> and 3.6  $\times$  10<sup>4</sup>  $\mathrm{M}^{-1}$  cm $^{-1}$  for the  $[\mathrm{Au}_{11}(\mathrm{S\text{-}BINAP})_4\mathrm{Cl}_2]^+$  and  $[\mathrm{Au}_{11}(\mathrm{S\text{-}BINAP})_4\mathrm{Br}_2]^+$  MPCs, respectively, at 430 nm.  $^{19}$ 

The UV-vis absorption spectra for [Au<sub>11</sub>(R/S-BI-NAP)<sub>4</sub>Cl<sub>2</sub>]<sup>+</sup> in chloroform and ethanol are compared in Figure 1b (see Figure S2 for additional solvents). Dispersion in protic solvents led to narrowing of the 330 and 430 nm absorption peaks. These peaks are assigned to a combination of core-to-ligand (430 nm) and ligand-to-ligand (330 nm) transitions, suggesting that the solvent has a pronounced effect on the structural inhomogeneity of the cluster-ligand shell. Interestingly, solvent-dependent absorption is not observed for [Au<sub>11</sub>(R/S-BINAP)<sub>4</sub>Br<sub>2</sub>]<sup>+</sup> (Figure 1b). Although changes in extinction were observed, line narrowing, which reflects the decreasing inhomogeneity, was observed only in the [Au<sub>11</sub>(R/ S-BINAP)<sub>4</sub>Cl<sub>2</sub>]<sup>+</sup> MPC. Because peak narrowing is observed for only the chlorinated clusters in protic solvents, the effect is attributed to hydrogen bonding between the solvent hydrogen and the MPC axial chloride, which leads to reduced structural inhomogeneity. Because of high electron densities, the halides of metal-halide bonds serve as hydrogen-bond acceptors in inorganic molecules. 25,26 Although hydrogen bonding in metal halides is possible for both chlorine and bromine atoms, hydrogen bonds are longer (by  $\approx 0.02$  Å) and weaker for bromide complexes. <sup>25</sup> Although this is only a 3% bond-length change, the small structural difference seemingly determines if strong hydrogen-bonding networks are formed. For MPCs, the axial chloride can act as a hydrogen-bond acceptor when the cluster is dispersed in a protic solvent that serves as a hydrogen-bond donor. Bromide-solvent hydrogen bonding is weaker because of the larger radius and smaller electronegativity of the bromine atom. Hence, cluster-solvent interactions can be modified through the choice of axial halogen atoms.

Time-dependent UV—vis absorption of both clusters was measured (Figure S3). No changes to  $[Au_{11}(R/S-BI-NAP)_4Cl_2]^+$  absorption were observed in the range of 2–6 min, regardless of the solvent. However, the narrowed absorption of the 330 and 430 nm peaks was observed by 3 h. This time dependence supports the idea that hydrogen bonding, rather than dielectric effects, causes absorption peak narrowing. The time dependence is attributed to gradual nanocluster—solvent hydrogen-bond formation. No time-dependent differences in hydrogen-bond formation between ethanol and methanol were resolved (Figure S3). As expected, the absorption spectra of MPCs in toluene showed no time-dependent changes (Figure S3c).

To understand the influence of hydrogen bonding on nanocluster optical properties, PL was measured for  $[Au_{11}(R/S-BINAP)_4Cl_2]^+$  in both protic and aprotic solvents. The data depicted in Figure 1c show that the  $[Au_{11}(R/S-BINAP)_4Cl_2]^+$  PL intensity is significant when it is dispersed in protic solvents but negligible in aprotic solvents. Furthermore, PL from the  $[Au_{11}(R/S-BINAP)_4Br_2]^+$  MPC was not detectable regardless of the dispersing solvent (Figure S4). MPC solutions were prepared such that the absorption at the excitation wavelength

(532 nm) was comparable; excitation fluxes were the same for all measurements. Hence, the stronger PL for  $[Au_{11}(R/S-BINAP)_4Cl_2]^+$  in protic systems reflected solvent-induced changes to MPC emission rates. The increased emission in protic solvents can be explained by the expression

emission rate (s<sup>-1</sup>) 
$$\propto \frac{k_{\rm rad}}{k_{\rm rad} + k_{\rm nr}}$$
 (1)

where  $k_{\rm rad}$  is the radiative decay rate and  $k_{\rm nr}$  is the nonradiative decay rate.  $k_{rad}$  is not expected to change due to the lack of solvent-dependent changes in the absorption peak centers, as well as previous data showing that halogen species are generally resistant to changes in  $k_{rad}$ , but with more sensitive responses to nonradiative decay.<sup>27</sup> Because  $k_{\text{rad}}$  is not expected to change, solvent-mediated changes to  $k_{nr}$  are hypothesized to induce the increased emission rate upon [Au<sub>11</sub>(R/S-BINAP)<sub>4</sub>Cl<sub>2</sub>]<sup>+</sup> dispersion in protic solvents. One possible explanation for reconciling both the narrowed absorption peaks and the increased emission by [Au<sub>11</sub>(R/S-BINAP)<sub>4</sub>Cl<sub>2</sub>]<sup>+</sup> in protic solvents is that  $k_{\rm nr}$  is decreased due to increased cluster rigidity arising from hydrogen bonding, which suppresses nonradiative vibrational relaxation pathways. Furthermore, the PL excitation spectrum of the [Au<sub>11</sub>(R/S-BINAP)<sub>4</sub>Cl<sub>2</sub>]<sup>+</sup> MPC dispersed in ethanol is shown in Figure S5. The PL excitation spectrum shows peaks in locations similar to those of the UV-vis spectrum.

Raman spectroscopy was carried out to examine the impact of hydrogen bonding on the MPC vibrational spectra. Raman spectra for [Au<sub>11</sub>(R/S-BINAP)<sub>4</sub>Cl<sub>2</sub>]<sup>+</sup> in both solvent types are shown in Figure S6. Prominent Raman scattering intensity was detected in the frequency range of 90–100 cm<sup>-1</sup> for a protic solvent dispersion. This frequency range corresponds to Au–Cl stretching, which has been observed for phosphine-protected Au<sub>8</sub>. MPCs in aprotic solvents exhibit dampened Raman signals, attributed to inhomogeneous vibrational mode broadening. In other words, the structural rigidity provided by the cluster-to-solvent Cl–H bonding network resulted in more distinct Au–Cl stretching signals. Hence, the low-frequency Raman measurements are consistent with the UV–vis and PL results, which indicate strong solvent–cluster hydrogen bonding interactions occur in protic solvents.

To determine if nanocluster-solvent hydrogen bonding influenced the nonradiative dynamics of [Au<sub>11</sub>(R/S-BI-NAP)<sub>4</sub>X<sub>2</sub>]<sup>+</sup>, MPC electronic relaxation dynamics were studied using femtosecond time-resolved transient absorption spectroscopy (fsTAS). The fsTAS spectra of [Au<sub>11</sub>(R/S-BINAP)<sub>4</sub>Cl<sub>2</sub>]<sup>+</sup> in both protic and aprotic solvents were dominated by excited-state absorption, which spanned the entire probe detection range (Figure 2a and Figure S7). However, a negative amplitude feature centered at 650 nm was detected superimposed on the broad ESA for [Au<sub>11</sub>(R/S-BINAP)<sub>4</sub>Cl<sub>2</sub>]<sup>+</sup> in protic solvents (Figure 2a). The 650 nm signal is in good agreement with the calculated HOMO-LUMO transition of this nanocluster. 23 A ratio of the 650 nm negative polarity to ESA amplitude remained constant as the probe power was systematically changed. On the basis of the absence of probe power sensitivity (Figure S8b), this 650 nm feature is assigned to HOMO-LUMO bleaching rather than stimulated emission. Consistent with the PL data depicted in Figure 1c, transient bleaching was not detected for  $[Au_{11}(R/S BINAP)_4Cl_2$  in aprotic solvents.

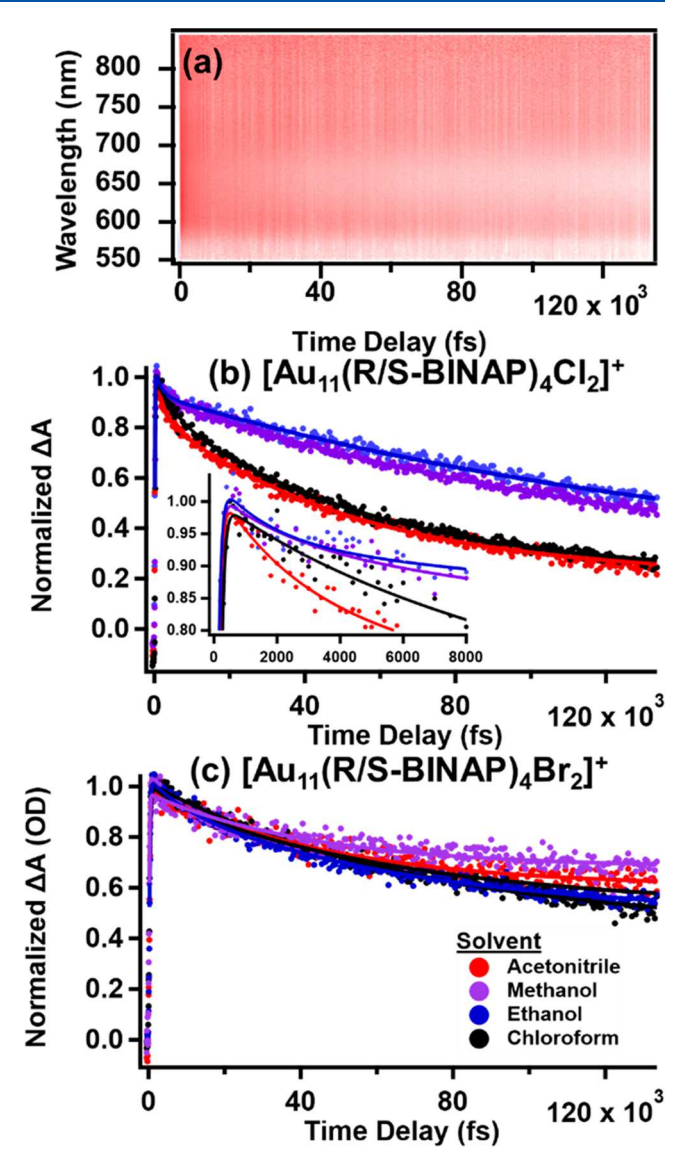


**Figure 2.** (a) fs-TA map of  $[Au_{11}(R/S-BINAP)_4Cl_2]^+$  dispersed in ethanol. (b) Transient absorption traces and fits of the  $[Au_{11}(R/S-BINAP)_4Cl_2]^+$  data from multiple solvents. The inset shows truncated transient absorption traces and fits to emphasize the short-time dynamics. (c) Transient absorption traces and fits of  $[Au_{11}(R/S-BINAP)_4Br_2]^+$  in multiple solvents. Data for additional solvents are shown in Figure S9.

Time-dependent  $[Au_{11}(R/S\text{-}BINAP)_4Cl_2]^+$  fsTAS signals are shown in Figure 2b. The data depicted in Figure 2b show distinct differences for  $[Au_{11}(R/S\text{-}BINAP)_4Cl_2]^+$  in protic (methanol and ethanol) and aprotic (acetonitrile and chloroform) solvents. The inset of Figure 2b is truncated to the first 8 ps of fsTAS signals for  $[Au_{11}(R/S\text{-}BINAP)_4Cl_2]^+$ . Figure 2b emphasizes a slow, ~4 ps fsTAS signal growth. As with UV—vis absorption and PL data, there were two categories for ultrafast dynamics.  $[Au_{11}(R/S\text{-}BINAP)_4Cl_2]^+$  in protic solvents showed more persistent signals over the fsTAS observation window, while the MPC in aprotic solvents showed more rapid signal decay. The  $[Au_{11}(R/S\text{-}BINAP)_4Br_2]^+$  fsTAS data were independent of solvent (Figure 2c).

The influence of the solvent on MPC relaxation dynamics was quantified by fitting the fsTAS data to the following consecutive-kinetics formalism:<sup>29</sup>

$$S(t) = \sum \operatorname{amp} \left( \frac{k_1}{k_1 - k_2} \right) (e^{-k_2 t} - e^{-k_1 t})$$
(2)

The accompanying kinetic model is provided in Figure 3a. Following metal-centered 575 nm excitation, carriers relax

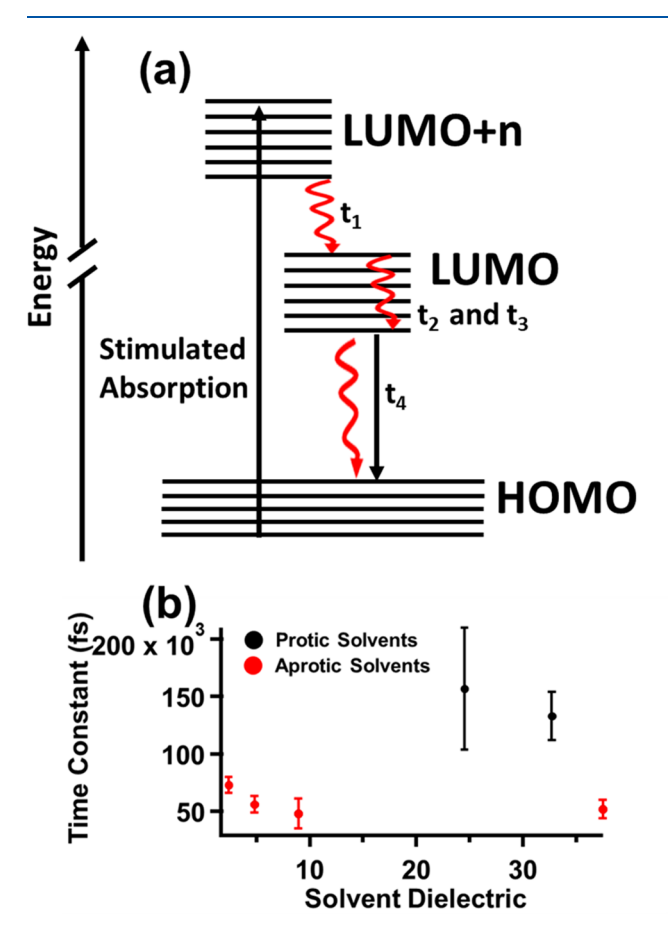


**Figure 3.** (a) Generalized excitation and relaxation mechanism for the  $[Au_{11}(R/S-BINAP)_4X_2]^+$  MPCs, where the HOMO is composed of gold core-based superatom P orbital states and the excited states, LUMO+n and LUMO, are both composed of gold core-based superatom D orbital states. (b) Plot of  $t_4$  vs solvent dielectric showing longer time constants for dispersion in protic solvents. Error bars are obtained from reduced  $\chi^2$  vs covariance analysis.<sup>33</sup>

from LUMO+n to LUMO by sub-100 fs internal conversion  $(t_1)$ . This step is general for atomically precise metal nanoclusters.  $^{30-32}$  Subsequently, intramolecular vibrational relaxation thermalizes the LUMO on an approximate 4 ps time scale, causing a decay  $(t_2)$  of ESA and growth  $(t_3)$  of the 650 nm bleach signals. The fourth component,  $t_4$ , tracks the competition between radiative and nonradiative relaxation from the LUMO to HOMO. Several other models were attempted for fitting the fsTAS signals. These included a series of simultaneous (i.e., nonconsecutive) relaxation steps and a combination of consecutive and simultaneous processes. Each model was evaluated using global and parameter specific  $\gamma^2$ tests, and inspection of residuals. Using these tests, it was clear that a series of simultaneous decay processes was not satisfactory; a consecutive-kinetics model was necessary to account for the data. Equation 2 provided the best fit for both brominated and chlorinated MPCs, regardless of the solvent choice. Hence, cluster-solvent interactions modified the rate

constants but did not change the relaxation model. The largest solvent effect occurred for  $t_4$ , HOMO-to-LUMO relaxation.

The solvent dependence of the  $t_4$  relaxation time constant is summarized in Figure 3b. Generally, for gold MPCs, solventdependent dynamics result from changes in the dielectric stabilization of charge-transfer states.<sup>34</sup> However, in this study, t<sub>4</sub> did not depend on the solvent dielectric but instead showed a binary response that was dictated by the ability of the solvent to hydrogen bond to the MPC halogen. A 2-fold increase in  $t_4$ was observed when [Au<sub>11</sub>(R/S-BINAP)<sub>4</sub>Cl<sub>2</sub>]<sup>+</sup> was dispersed in protic solvents. This increase in  $t_4$  is attributed to hydrogen bonding, which suppresses nonradiative vibrational relaxation of carriers from the LUMO to the HOMO. Because  $t_4$  includes both radiative and nonradiative decay (eq 1), less efficient vibration-mediated nonradiative relaxation increases the time constant. Similarly, less efficient vibrational relaxation increases the PL (Figure 2). Taken together, the complementary solvent dependencies of  $t_4$  and PL emission support the interpretation that [Au<sub>11</sub>(R/S-BINAP)<sub>4</sub>Cl<sub>2</sub>]<sup>+</sup> forms a Cl-H bond network in protic solvents, which impacts the photoinduced relaxation dynamics and optical properties of the MPC.

In summary, the influence of halogen-hydrogen bonding on the electronic relaxation dynamics and photoluminescence properties of  $[Au_{11}(R/S-BINAP)_4X_2]^+$ , where X = Cl, is described. [Au<sub>11</sub>(R/S-BINAP)<sub>4</sub>Cl<sub>2</sub>]<sup>+</sup> showed strong solventdependent responses, whereas [Au<sub>11</sub>(R/S-BINAP)<sub>4</sub>Br<sub>2</sub>]<sup>+</sup> did not. This nanocluster specificity is attributed to the greater affinity of the MPC axial chlorine atom to form a hydrogenbond network with protic solvents. As a consequence, the Hbonding network forms a rigid [Au<sub>11</sub>(R/S-BINAP)<sub>4</sub>Cl<sub>2</sub>]<sup>+</sup>solvent complex with reduced dynamic disorder when compared to dispersion in aprotic solvents or the brominated MPC variant. These conclusions are supported by mutually consistent electronic absorption and Raman scattering measurements, both of which exhibited narrowed line widths and increased signal intensities. Nanocluster-solvent hydrogen bonding also resulted in increased photoluminescence emission; PL was significant for only [Au<sub>11</sub>(R/S-BINAP)<sub>4</sub>Cl<sub>2</sub>]<sup>+</sup> dispersed in protic solvents. This effect was attributed to the decreased efficiency of vibrationally mediated nonradiative relaxation for the more rigid, hydrogen-bonded cluster-solvent species: increased rigidity reduced electron-vibrational coupling. These results are important, because they reveal a new structural parameter that can be used to modify the optical properties of metal nanoclusters. Furthermore, the results emphasize the importance of considering the first solvent layer as a structural component in the design of atomically precise nanoclusters.

# **EXPERIMENTAL METHODS**

Synthesis and Characterization of  $[Au_{11}(R/S\text{-}BINAP)_4X_2]^+$  MPCs. The synthesis of the  $[Au_{11}(R/S\text{-}BINAP)_4X_2]^+$  clusters was carried out using the protocol developed by Tsukuda et al.  $^{19}$   $[Au_{11}(R/S\text{-}BINAP)_4Cl_2]^+$  was synthesized from chloroauric acid trihydrate (>99.9%) that was obtained from Sigma-Aldrich.  $[Au_{11}(R/S\text{-}BINAP)_4Br_2]^+$  was synthesized from potassium tetrabromoaurate dihydrate (>99.99%) that was obtained from Thermo Fisher. Dimethyl sulfide (DMS) (>99%) was obtained from Sigma-Aldrich. S-BINAP was obtained from Sigma-Adrich. Sodium borohydride (>98%) was obtained from Thermo Fisher.

The bottom-up method was used to synthesize  $[Au_{11}(R/S-BINAP)_4X_2]^+$ . Specifically, to synthesize  $[Au_{11}(R/S-BI-BINAP)_4X_2]^+$ .

NAP)<sub>4</sub>Cl<sub>2</sub>]<sup>+</sup>, 55 mg of chloroauric acid trihydrate was dissolved in methanol before 0.5 mL of DMS was added dropwise. Immediately after the addition of DMS, a white precipitate began to form. For [Au<sub>11</sub>(R/S-BINAP)<sub>4</sub>Br<sub>2</sub>]<sup>+</sup> synthesis, 60 mg of potassium tetrabromoaurate trihydrate was substituted for chloroauric acid trihydrate. The solution for both halogenated clusters was stirred for 30 min before being washed with 10 mL of methanol, diethyl ether, and hexanes. The resulting white solid was then dissolved in dichloromethane (DCM) and placed under a nitrogen atmosphere. After the solution was cooled in an ice bath, 30 mg of BINAP dissolved in DCM was added dropwise to the AuX-DMS precursor mixture and the mixture stirred for 2 h. The solution was evaporated, and a white solid remained. Finally, the Au<sub>2</sub>X<sub>2</sub>BINAP precursor was dissolved in DCM, and 5 mg of NaBH4 was dissolved in ethanol before being added dropwise to the precursor solution. Immediately after the NaBH<sub>4</sub> was added, a change in the color to brown was observed; over the course of 2 h, the color of the solution gradually became darker. The reaction solution was then washed with 3 × 20 mL of Millipore water. The resulting solution was evaporated, and dark brown crystals with a typical yield of 85% were acquired.

The clusters were characterized via UV—vis spectroscopy and ESI-MS. UV—vis spectroscopy was carried out using an Aligent Cary 60 spectrophotometer and a quartz cuvette with a path length of 1 cm. ESI-MS was performed using a QExactive mass spectrometer in positive mode with an infusion rate of 5  $\mu$ L/min. A resolving power of 70 000 was used. To achieve a stable ion signal, a spray voltage of 3.5 kV, a capillary temperature of 300 °C, a sheath gas of 10 units, a probe heater of 70 °C, and an S-lens RF level of 50 were all used.

Raman Spectroscopy and Photoluminescence Measurements. Raman spectroscopy and photoluminescence measurements were carried out using a Horbia LabRAM HR Evolution instrument. An ultralow-loss fiber at 532 nm that was attenuated to 10% of the original power was used as an excitation source to avoid degradation. Samples dispersed in protic and aprotic solvents were prepared at concentrations of 5 mM on single concavity glass slides for measurements. Photoluminescence was measured from 550 to 1000 nm. Low-frequency Raman measurements were taken from 0 to 250 cm<sup>-1</sup> and subtracted from a solvent blank to acquire signals associated with vibrational modes that arose only from the cluster.

The time-dependent TAS signals were fit to the models described above using scripts written in Igor. Reduced  $\chi^2$  analysis, global  $\chi^2$  analysis, and residuals were used to identify the best fit results and to verify if the fit results were unique solutions for the data.

Femtosecond Transient Absorption Spectroscopy. Femtosecond transient absorption spectroscopy was performed using a setup that has been previously described. Briefly, the 1040 nm fundamental from a 100 kHz ytterbium amplifier was used to seed a noncollinear optical parametric amplifier (NOPA) (Spectra Physics Spirit-NOPA). The NOPA was used to generate visible pulses at 575 nm with a full width at half-maximum of 33 nm. The pulses were then compressed with chirped mirrors and collimated before being split by a 95/5 beam splitter for the pump and probe, respectively. The pump was chopped by a 2DES quick visible setup from Phase Tech, which consists of a TeO<sub>2</sub> acousto-optic modulator, before being sent through a delay stage to generate the pump probe

time delay. The time delay stage allowed for measurements to be carried out from -500 fs to 135 ps. The pump and probe beams were then focused on the sample using a parabolic mirror in which temporal and spatial overlap are achieved to generate a signal. Typical temporal instrument response functions with the solvents were 62 fs in duration, correlating with 39 fs pulse durations at the sample. Pump pulse energies at the sample were 10 nJ. The probe was then transmitted onto a Princeton Instruments SP2150i array detector. The probe wavelength range spanned 550-600 nm for all nearly degenerate measurements. Broadband transient absorption measurements were carried out using the same pump pulse but with a white light probe generated from the 1040 nm fundamental and a sapphire crystal. After generation, the white light was collimated and compressed using chirped mirrors. Probe wavelengths using the broadband probe ranged from 540 to 840 nm. Samples for this experiment were prepared at least 30 min before laser excitation to ensure that the hydrogen bonding network had formed. All samples were prepared at a concentration of 3 mM for all measurements and were housed in a 2 mm quartz cuvette.

### ASSOCIATED CONTENT

## Supporting Information

The Supporting Information is available free of charge at https://pubs.acs.org/doi/10.1021/acs.jpclett.4c00197.

Experimental procedures, ESI-MS data, Raman data, additional UV-vis spectra, and fsTAS spectra (PDF)

## AUTHOR INFORMATION

#### **Corresponding Author**

Kenneth L. Knappenberger, Jr. – Department of Chemistry, The Pennsylvania State University, University Park, Pennsylvania 16802, United States; oorcid.org/0000-0003-4123-3663; Email: klk260@psu.edu

#### **Authors**

Daniel J. Heintzelman – Department of Chemistry, The Pennsylvania State University, University Park, Pennsylvania 16802, United States; ⊚ orcid.org/0009-0002-2487-3845 Seth A. Nelson – Department of Chemistry, The Pennsylvania State University, University Park, Pennsylvania 16802, United States

Complete contact information is available at: https://pubs.acs.org/10.1021/acs.jpclett.4c00197

## **Funding**

D.J.H. was supported by a National Science Foundation (NSF) award to K.L.K. (CHE-2204190). S.A.N. was supported by NSF Grants DMR 1851987 and MRSEC (NSF DMR 2011839). A portion of this work was based on research supported by the Air Force Office of Scientific Research (FA9550-22-1-0402).

#### Notes

The authors declare no competing financial interest.

#### ACKNOWLEDGMENTS

The authors acknowledge the Penn State Materials Research Institute (MRI) and Dr. Maxwell Weatherington for Raman and photoluminescence support. The authors acknowledge Dr. Tatiana Laremore for ESI-MS support.

#### REFERENCES

- (1) Zheng, J.; Petty, J. T.; Dickson, R. M. High Quantum Yield Blue Emission from Water-Soluble Au8 Nanodots. *J. Am. Chem. Soc.* **2003**, 125 (26), 7780–7781.
- (2) Lee, D.; Donkers, R. L.; Wang, G.; Harper, A. S.; Murray, R. W. Electrochemistry and Optical Absorbance and Luminescence of Molecule-like Au38 Nanoparticles. *J. Am. Chem. Soc.* **2004**, *126* (19), 6193–6199.
- (3) Wang, G.; Guo, R.; Kalyuzhny, G.; Choi, J.-P.; Murray, R. W. NIR Luminescence Intensities Increase Linearly with Proportion of Polar Thiolate Ligands in Protecting Monolayers of Au38 and Au140 Quantum Dots. J. Phys. Chem. B 2006, 110 (41), 20282–20289.
- (4) Petty, J. T.; Fan, C.; Story, S. P.; Sengupta, B.; St. John Iyer, A.; Prudowsky, Z.; Dickson, R. M. DNA Encapsulation of 10 Silver Atoms Producing a Bright, Modulatable, Near-Infrared-Emitting Cluster. *J. Phys. Chem. Lett.* **2010**, *1* (17), 2524–2529.
- (5) Petty, J. T.; Fan, C.; Story, S. P.; Sengupta, B.; Sartin, M.; Hsiang, J.-C.; Perry, J. W.; Dickson, R. M. Optically Enhanced, Near-IR, Silver Cluster Emission Altered by Single Base Changes in the DNA Template. *J. Phys. Chem. B* **2011**, *115* (24), 7996–8003.
- (6) Petty, J. T.; Story, S. P.; Hsiang, J.-C.; Dickson, R. M. DNA-Templated Molecular Silver Fluorophores. *J. Phys. Chem. Lett.* **2013**, 4 (7), 1148–1155.
- (7) Green, T. D.; Yi, C.; Zeng, C.; Jin, R.; McGill, S.; Knappenberger, K. L. Temperature-Dependent Photoluminescence of Structurally-Precise Quantum-Confined Au <sub>25</sub> (SC <sub>8</sub> H <sub>9</sub>) <sub>18</sub> and Au <sub>38</sub> (SC <sub>12</sub> H <sub>25</sub>) <sub>24</sub> Metal Nanoparticles. *J. Phys. Chem. A* **2014**, *118* (45), 10611–10621.
- (8) Khatun, E.; Ghosh, A.; Chakraborty, P.; Singh, P.; Bodiuzzaman, M.; Ganesan, P.; Nataranjan, G.; Ghosh, J.; Pal, S. K.; Pradeep, T. A Thirty-Fold Photoluminescence Enhancement Induced by Secondary Ligands in Monolayer Protected Silver Clusters. *Nanoscale* **2018**, *10* (42), 20033–20042.
- (9) Han, Z.; Dong, X.-Y.; Luo, P.; Li, S.; Wang, Z.-Y.; Zang, S.-Q.; Mak, T. C. W. Ultrastable Atomically Precise Chiral Silver Clusters with More than 95% Quantum Efficiency. *Sci. Adv.* **2020**, *6* (6), No. eaay0107.
- (10) Herbert, P. J.; Ackerson, C. J.; Knappenberger, K. L., Jr. Size-Scalable Near-Infrared Photoluminescence in Gold Monolayer Protected Clusters. *J. Phys. Chem. Lett.* **2021**, *12* (31), 7531–7536.
- (11) Herbert, P. J.; Knappenberger, K. L., Jr. Spin-Polarized Photoluminescence in Au25(SC8H9)18 Monolayer-Protected Clusters. *Small* **2021**, *17* (27), No. 2004431.
- (12) Aikens, C. M. Effects of Core Distances, Solvent, Ligand, and Level of Theory on the TDDFT Optical Absorption Spectrum of the Thiolate-Protected Au25 Nanoparticle. *J. Phys. Chem. A* **2009**, *113* (40), 10811–10817.
- (13) Jeffries, W. R.; Malola, S.; Tofanelli, M. A.; Ackerson, C. J.; Häkkinen, H.; Knappenberger, K. L., Jr. Coherent Vibrational Dynamics of Au144(SC8H9)60 Nanoclusters. *J. Phys. Chem. Lett.* **2023**, *14* (29), 6679–6685.
- (14) Hartland, G. V. Optical Studies of Dynamics in Noble Metal Nanostructures. *Chem. Rev.* **2011**, *111* (6), 3858–3887.
- (15) Zhong, Y.; Zhang, J.; Li, T.; Xu, W.; Yao, Q.; Lu, M.; Bai, X.; Wu, Z.; Xie, J.; Zhang, Y. Suppression of Kernel Vibrations by Layer-by-Layer Ligand Engineering Boosts Photoluminescence Efficiency of Gold Nanoclusters. *Nat. Commun.* **2023**, *14* (1), 658.
- (16) Liu, Z.; Luo, L.; Jin, R. Visible to NIR-II Photoluminescence of Atomically Precise Gold Nanoclusters. *Adv. Mater.* **2024**, *36*, 2309073.
- (17) Jin, R.; Zeng, C.; Zhou, M.; Chen, Y. Atomically Precise Colloidal Metal Nanoclusters and Nanoparticles: Fundamentals and Opportunities. *Chem. Rev.* **2016**, *116* (18), 10346–10413.
- (18) Zhu, M.; Aikens, C. M.; Hollander, F. J.; Schatz, G. C.; Jin, R. Correlating the Crystal Structure of A Thiol-Protected Au25 Cluster and Optical Properties. *J. Am. Chem. Soc.* **2008**, *130* (18), 5883–5885.
- (19) Yanagimoto, Y.; Negishi, Y.; Fujihara, H.; Tsukuda, T. Chiroptical Activity of BINAP-Stabilized Undecagold Clusters. *J. Phys. Chem. B* **2006**, *110* (24), 11611–11614.

- (20) Provorse, M. R.; Aikens, C. M. Origin of Intense Chiroptical Effects in Undecagold Subnanometer Particles. *J. Am. Chem. Soc.* **2010**, *132* (4), 1302–1310.
- (21) Takano, S.; Tsukuda, T. Amplification of the Optical Activity of Gold Clusters by the Proximity of BINAP. *J. Phys. Chem. Lett.* **2016**, 7 (22), 4509–4513.
- (22) Shinjo, N.; Takano, S.; Tsukuda, T. Effects of  $\pi$ -Electron Systems on Optical Activity of Au11 Clusters Protected by Chiral Diphosphines. *Bulletin of the Korean Chemical Society* **2021**, 42 (9), 1265–1268.
- (23) Karimova, N. V.; Aikens, C. M. Chiroptical Activity in BINAP-and DIOP-Stabilized Octa- and Undecagold Clusters. *J. Phys. Chem. C* **2018**, *122* (20), 11051–11065.
- (24) Qin, Z.; Zhao, D.; Zhao, L.; Xiao, Q.; Wu, T.; Zhang, J.; Wan, C.; Li, G. Tailoring the Stability, Photocatalysis and Photoluminescence Properties of Au11 Nanoclusters via Doping Engineering. *Nanoscale Adv.* **2019**, *1* (7), 2529–2536.
- (25) Brammer, L.; Bruton, E. A.; Sherwood, P. Understanding the Behavior of Halogens as Hydrogen Bond Acceptors. *Cryst. Growth Des.* **2001**, *1* (4), 277–290.
- (26) Aullón, G.; Bellamy, D.; Guy Orpen, A.; Brammer, L.; Bruton, E. A. Metal-Bound Chlorine Often Accepts Hydrogen Bonds. *Chem. Commun.* 1998, 6, 653–654.
- (27) Lakowicz, J. R., Ed. Principles of Fluorescence Spectroscopy; Springer US: Boston, 2006.
- (28) Kato, M.; Shichibu, Y.; Ogura, K.; Iwasaki, M.; Sugiuchi, M.; Konishi, K.; Yagi, I. Terahertz Raman Spectroscopy of Ligand-Protected Au8 Clusters. J. Phys. Chem. Lett. 2020, 11 (19), 7996—8001
- (29) Pedersen, S.; Zewail, A. Femtosecond Real Time Probing of Reactions XXII Kinetic Description of Probe Absorption Fluorescence Depletion and Mass Spectrometry. *Mol. Phys.* **1996**, *89* (5), 1455–1502.
- (30) Stoll, T.; Sgrò, E.; Jarrett, J. W.; Réhault, J.; Oriana, A.; Sala, L.; Branchi, F.; Cerullo, G.; Knappenberger, K. L., Jr. Superatom State-Resolved Dynamics of the Au25(SC8H9)18— Cluster from Two-Dimensional Electronic Spectroscopy. *J. Am. Chem. Soc.* **2016**, *138* (6), 1788–1791.
- (31) Zhao, T.; Herbert, P. J.; Zheng, H.; Knappenberger, K. L., Jr. State-Resolved Metal Nanoparticle Dynamics Viewed through the Combined Lenses of Ultrafast and Magneto-Optical Spectroscopies. *Acc. Chem. Res.* **2018**, *51* (6), 1433–1442.
- (32) Miller, S. A.; Womick, J. M.; Parker, J. F.; Murray, R. W.; Moran, A. M. Femtosecond Relaxation Dynamics of Au25L18—Monolayer-Protected Clusters. *J. Phys. Chem. C* **2009**, *113* (22), 9440–9444.
- (33) McArthur, E. A.; Morris-Cohen, A. J.; Knowles, K. E.; Weiss, E. A. Charge Carrier Resolved Relaxation of the First Excitonic State in CdSe Quantum Dots Probed with Near-Infrared Transient Absorption Spectroscopy. *J. Phys. Chem. B* **2010**, *114* (45), 14514–14520.
- (34) Yi, C.; Zheng, H.; Herbert, P. J.; Chen, Y.; Jin, R.; Knappenberger, K. L. Ligand- and Solvent-Dependent Electronic Relaxation Dynamics of Au25(SR)18— Monolayer-Protected Clusters. *J. Phys. Chem. C* **2017**, *121* (44), 24894—24902.
- (35) Jeffries, W. R.; Fagan, A. M.; Schaak, R. E.; Knappenberger, K. L., Jr. Influence of Band Alignment on Electronic Relaxation in Plasmonic-Semiconductor Hybrid Nanoparticles. *J. Phys. Chem. C* **2022**, *126*, 8384–8392.